JMEPEG (2022) 31:1728–1736
https://doi.org/10.1007/s11665-021-06332-9

1059-9495/$19.00

Investigation on Hydrogen Embrittlement Sensitivity of Hot-Rolled and Annealed Microstructure to AISI 430 Ferritic Stainless Steel

Tao Wang, Wenjie Lv, Wentao Xiao, Kun Wang, Huiyun Zhang, and Wei Liang

Submitted: 15 July 2021 / Revised: 7 September 2021 / Accepted: 11 September 2021 / Published online: 12 November 2021

This paper studied the influence of hot rolling and annealing processes on the hydrogen embrittlement sensitivity of AISI 430 ferritic stainless steel and the changes in hydrogen-induced fracture modes through electrochemical hydrogen charging experiments. The tensile test results show that the hot-rolled specimen has the highest hydrogen embrittlement sensitivity, and the highest yield strength and tensile strength. After the heat treatment, the yield strength of all specimens was significantly increased after hydrogen charging, which was attributed to the hydrogen-induced dislocation pinning effect. The fracture morphology analysis revealed that the hot-rolled specimen was dominated by intergranular fracture, accompanied by cleavage fracture, predominantly by the hydrogen-enhanced decohesion (HEDE) mechanism, while the fracture modes of annealed specimen were cleavage fracture and quasi-cleavage fracture due to the hydrogen-enhanced localized plasticity (HELP) and hydrogen-enhanced decohesion (HEDE) mechanisms.

Keywords 430 ferritic stainless steel, fracture mechanism, hydrogen embrittlement, mechanical properties

1. Introduction

As a new type of green energy, hydrogen has gradually replaced traditional coal mine energy (Ref 1). Due to the increase in the transportation volume and transportation scope of hydrogen pipelines, the requirements for the mechanical properties of pipeline materials have been greatly improved. However, high-strength steel is more susceptible to hydrogen embrittlement (Ref 2-5). Hydrogen penetration of metal significantly deteriorates the mechanical properties of the material, especially the reduction in plasticity, which limits the application and development of high-strength steels (Ref 6-8).

Many research works have identified that hydrogen embrittlement (HE) is due to the interaction between hydrogen and the internal microstructure of the material (Ref 9-11). Two main models for explaining the changes in the fracture mode of hydrogen-induced materials were proposed in the twentieth century: (1) hydrogen-enhanced localized plasticity (HELP) (Ref 12), (2) hydrogen-enhanced decohesion (HEDE) (Ref 13). HELP mechanism is based on the fact that hydrogen reduces the critical stress intensity of dislocation movement through hydrogen, which leads to an increase in dislocation mobility (Ref 15). For the HEDE mechanism, the accumulation of hydrogen at high triaxial stress positions leads to weakening of atomic bonds beyond the critical hydrogen concentration (Ref 14). Although the coexistence of different hydrogen embrittlement mechanisms has been observed in metallic materials (Ref 16-18), the interaction between them (which mechanism is the dominant one) is still a challenging and critical issue (Ref 19, 20).

FSS is widely used in electrical appliances, marine environment materials and pipeline transportation due to its good corrosion resistance, excellent mechanical properties and low price. As the basic structure of high-strength steel, the HE mechanism of ferrite is still in the research stage. Therefore, in the present study, the HE performance of AISI 430 FSS was investigated by using rolling, annealing and tensile test. By comparing the mechanical properties and fracture morphology changes before and after hydrogen charging, the relationship among the rolling and annealing microstructure of AISI 430 FSS and hydrogen embrittlement sensitivity (HES_H) was also discussed.

2. Experimental

2.1 Materials and Experimental Process

The material used for this study was AISI 430 FSS with the chemical composition of 0.04% C, 0.29% Si, 0.35% Mn, 0.023% P, 0.003% S, 16.21% Cr, 0.14% Ni and balance Fe wt.% (represented by melting analysis). JMatPro software was employed to perform phase zone thermal simulation on the

Tao Wang, Wenjie Lv, Wentao Xiao, and **Huiyun Zhang**, College of Materials Science and Engineering, Taiyuan University of Technology, Taiyuan 030024, People's Republic of China; **Kun Wang**, College of Materials Science and Engineering, Taiyuan University of Technology, Taiyuan 030024, People's Republic of China; and Shanxi Key Laboratory of Advanced Magnesium-based Materials, Taiyuan University of Technology, Taiyuan 030024, People's Republic of China; and **Wei Liang**, College of Materials Science and Engineering, Taiyuan University of Technology, Taiyuan 030024, People's Republic of China; Shanxi Key Laboratory of Advanced Magnesium-based Materials, Taiyuan University of Technology, Taiyuan 030024, People's Republic of China; and Instrumental Analysis Center, Taiyuan University of Technology, Taiyuan 030600, People's Republic of China. Contact e-mail: liangwei@tyut.edu.cn.

original sheet to determine the heat treatment temperature, as shown in Fig. 1(a). The original 2.86mm annealed sheet was subjected to the heat treatment procedures described in Fig. 1b. The original sheet (O) was first subjected to a rolling process at 850°C for 10 minutes, after which the original sheet was quenched in air (the cooling rate is 5 °C/s-10 °C/s), in which we got the rolled specimens (HR) with a thickness of 2mm. After one pass, the corresponding rolling reduction is 30%. The next step was that the rolled sheet was annealed at 940°C for 10 minutes before final quenching in air to obtain the roll-annealed specimens (HR/A). The geometry of all specimens used to conduct the tensile tests is shown in Fig. 2(a), and the dimensions of specimens used to microstructure analysis are shown in Fig. 2(b).

2.2 Electrochemical Hydrogen Charging and Tensile Tests

Hydrogen was introduced into the FSS material by traditional electrochemical hydrogen charging experiment. The cathode of the electrochemical system was the tensile specimens, while metal platinum sheet connected to anode. The samples for electrochemical hydrogen charging experiment were lightly grounded with a 2000 grade SiC paper to eliminate impurities on the surface of specimens caused by the machining process. This process was performed in 300 ml of sodium hydroxide solution (1 mol/l), poisoned with thiourea (1 g/l) as hydrogen recombination inhibitor, at room temperature. A constant current density of 50 mA/cm^2 was maintained with an DC power source (MS-605D), and the hydrogen charging time was 8 h.

The tensile properties of AISI 430 FSS specimens produced after different processing treatments were examined before and after hydrogen charging. Before the tensile tests, the surface of the sample was pretreated with 2000# SiC paper to obtain a smooth and flat tensile sample. Tensile tests under strain rate mode (1×10^{-4} s^{-1}) were performed at air temperature, and an extensometer with a gauge length of 25mm was installed to calculate the total elongation capacity of specimens.

Plastic loss is the main manifestation of material HE; therefore, the hydrogen embrittlement sensitivity (HES_H) of the material can be characterized by calculating the elongation loss rate before and after the tensile sample is charged with hydrogen. HES_H can be obtained by Eq 1:

$$HES_H = \frac{\delta_0 - \delta_H}{\delta_0} \times 100\% \quad \text{(Eq 1)}$$

where δ_0 and δ_H represent the elongation of the tensile specimens before and after hydrogen charging, respectively. The larger the hydrogen embrittlement sensitivity value, the worse the material's resistance to hydrogen embrittlement, and the more sensitive the microstructure to hydrogen.

2.3 Observation of Microstructure and Fracture Morphology

Microstructure evaluation and fracture morphology analysis of the specimens before and after hydrogen charging were conducted at each stage of the treatment process using a field emission scanning electron microscopy (FE-SEM, Tescan Mira 3) equipped with an Oxford energy-dispersive spectroscopy (EDS) and an electron backscattered diffraction (EBSD) detector. The EBSD scans were performed with a step size of 0.5 μm at an accelerating voltage of 20 kV, and the EBSD result was post-processed with the Channel 5 software in the AZTEC 2.0 software. For EBSD study, specimens were polished with SiC paper and electrolyzed with perchloric acid alcohol solution at -30°C for 70s.

3. Result

3.1 Microstructure

The microstructural transformations after thermal treatments are shown in Fig. 3 (SEM topography and EDS spectra) and Fig. 4 (EBSD data analysis results). The microstructures of the

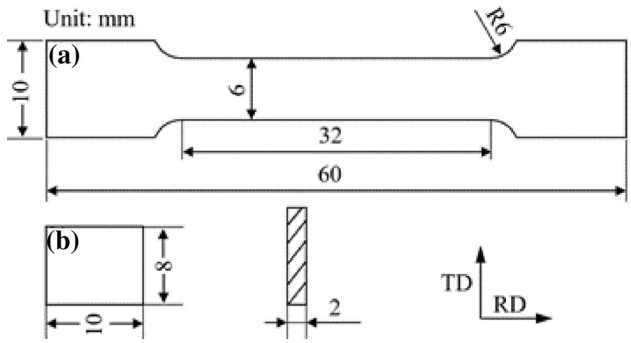

Fig. 2 (a) The geometry of all tensile specimens, (b) the dimensions of microstructure analysis specimens

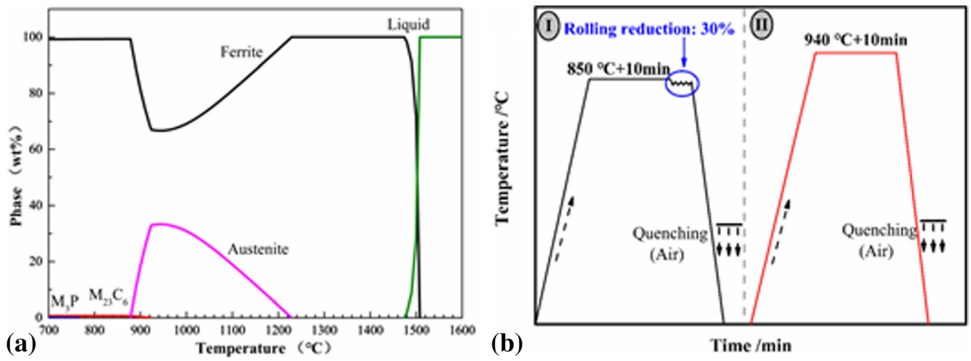

Fig. 1 (a) Thermal simulation phase map and (b) schematic representation of heat treatment process

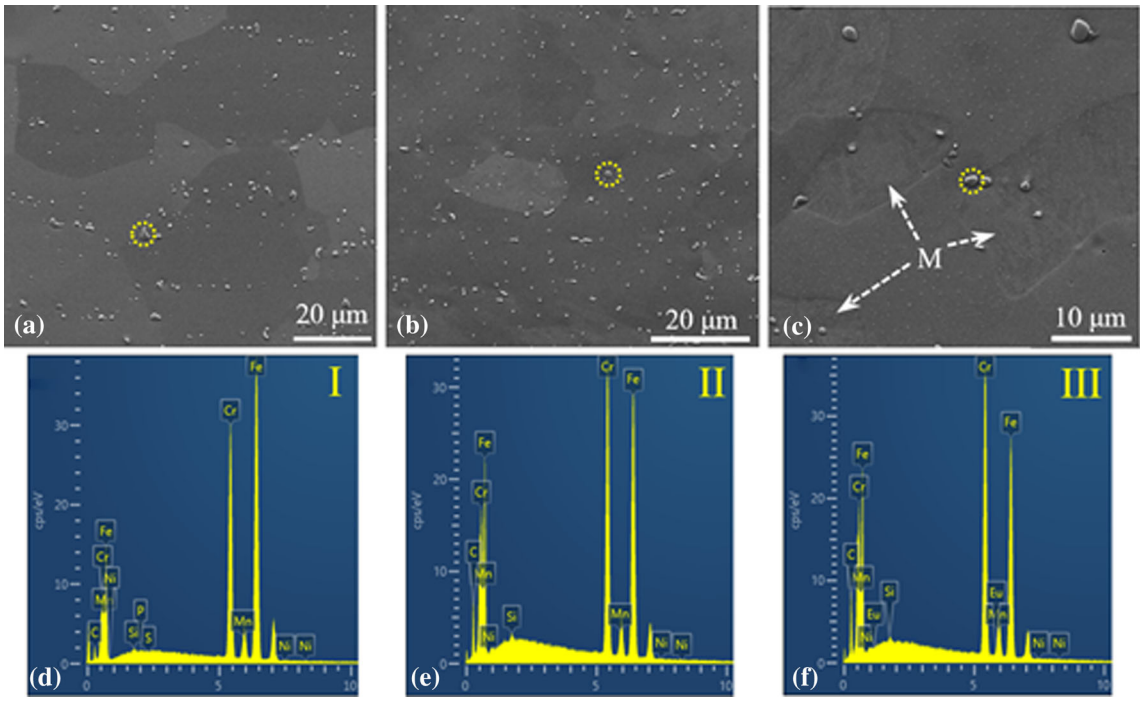

Fig. 3 SEM topography and EDS spectra of specimens in different states. (a) Original specimen, (b) hot-rolled specimen, (c) annealed specimen; (d-f), respectively, correspond to the energy spectrum of the precipitate in the yellow circle in (a-c)

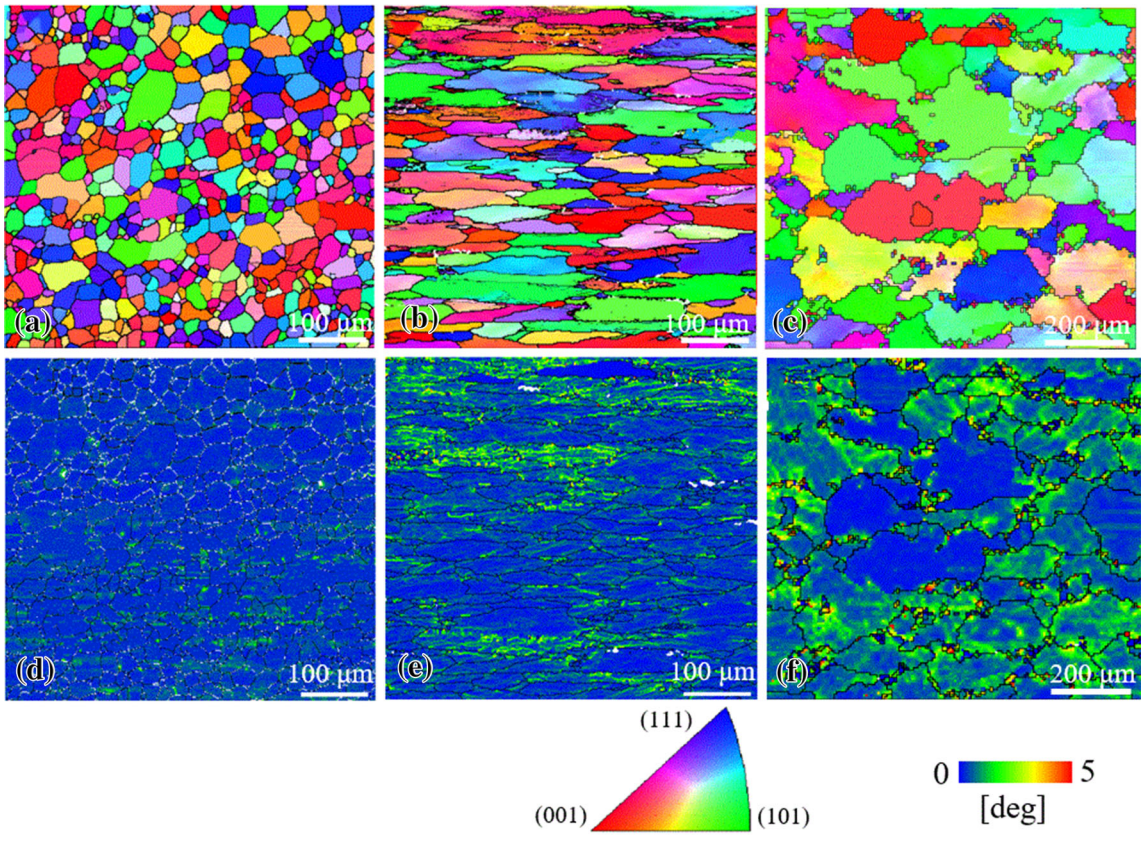

Fig. 4 EBSD data analysis results of specimens in different states. (a) Original specimen, (b) hot-rolled specimen, (c) annealed specimen; (a-c) IPF images, (d-f) KAM images

original specimen and the hot-rolled sample are pure ferrite structure and precipitates dispersed in the matrix as indicated in Fig. 3a and b. The microstructure morphology displayed two different microstructures, namely the ferrite matrix and the martensite phase (indicated by the white box), as shown in Fig. 3c. The EDS spectra of the precipitates in the matrix in the three states are shown in Fig. 3d, e and f, while the EDS data analysis results of precipitates as shown in Table 1, respectively, indicating that the precipitates are $(FeCr)_{23}C_6$. The ferrite grains in the uniform equiaxed state and the elongated ferrite grains produced after hot rolling are observed in Fig. 4a and b, respectively. The ferrite grains of the hot-rolled sample are transformed into an equiaxed state after annealing in Fig. 4c. Compared with the original specimen, in which the mean grain sizes are between 10 and 30 μm, the grain size of hot-rolled and annealed specimens increased significantly. The grain size of annealed specimen is 66 μm.

Figure 4c, d and e shows the Kernel Average Misorientation (KAM) map of specimens in different states. It can be seen from the map that KAM value of the original sample was the lowest, a higher KAM value was observed in both hot-rolled and annealed specimens, which attribute to deformation and martensite transformation. Jedrychowski et al. (Ref 21) expressed the kernel average misorientation (KAM) using EBSD data as follows:

$$\mathrm{KAM}(\mathrm{point}\, j) = \frac{\Sigma_{k=1}^{N} \omega(g_i, g_j)}{N} \quad \text{(Eq 2)}$$

where N is the sum of adjacent EBSD points that satisfy the threshold misorientation value (usually 5°), and $\omega(g_i, g_j)$ is the difference between the orientation of the neighboring point g_i and the orientation of point j itself g_j, i.e., the misorientation angle. In general, ρ^{GND} can be expressed according to the formula (Ref 22):

$$\rho^{\mathrm{GND}} = \frac{2\upsilon}{ub} \quad \text{(Eq 3)}$$

Table 1 EDS data analysis results of precipitates

Sample	Element content, wt.%		
	Fe	Cr	C
I	60.8	31.6	6.80
II	56.4	35.5	7.40
III	50.2	39.3	8.90

where u is the unit length and b is the magnitude of the Burgers vector, υ is the misorientation angle. The KAM, which can be directly retrieved from EBSD data, is selected as the measure for the local misorientations. According to the report by Liu and Hansen (Ref 23), the stored deformation energy is proportional to the density of ρ^{GND}. Therefore, the KAM is sensitive to the stored energy. The higher KAM value obtained from the EBSD data corresponds to a higher geometrically necessary dislocations (ρ^{GND}) (Ref 22).

3.2 Mechanical Properties and Hydrogen Embrittlement Sensitivity

Figure 5a shows representative stress–strain curves of specimens before and after hydrogen charging in different states and standard deviation of mechanical properties in Fig. 5b. The tensile properties of each specimen before and after hydrogen charging are presented in Table 2. It is visible that there are obvious differences in the mechanical properties of samples in different states before and after hydrogen charging. The original sample has the best plasticity (37.08%), while the hot-rolled sample has the highest yield strength (395 MPa) and ultimate tensile strength (470 MPa). The hot-rolled specimens after annealing exhibited no outstanding aspect in the mechanical properties, which attribute to the abnormal growth of ferrite grains. After hydrogen charging, a significant reduction in the ductility occurred in all specimens. However, the HES_H of the hot-rolled specimen was significantly higher than that of the other two state specimens, indicating that hydrogen is more sensitive to stress state (Ref 24, 25). It is worth noting that the yield strength of hot-rolled and annealed samples is significantly increased after hydrogen charging, which may be attributed to the effect of hydrogen on

Table 2 Mechanical performance data of specimens before and after hydrogen charging under different conditions

Material status	YS, MPa	UTS, MPa	δ_A, %	HES_H, %
O	285	430	37.08	24.91
O-H	285	425	27.84	
HR	395	470	12.34	67.50
HR-H	440	495	4.01	
HR/A	240	435	21.03	56.73
HR/A-H	280	415	9.10	

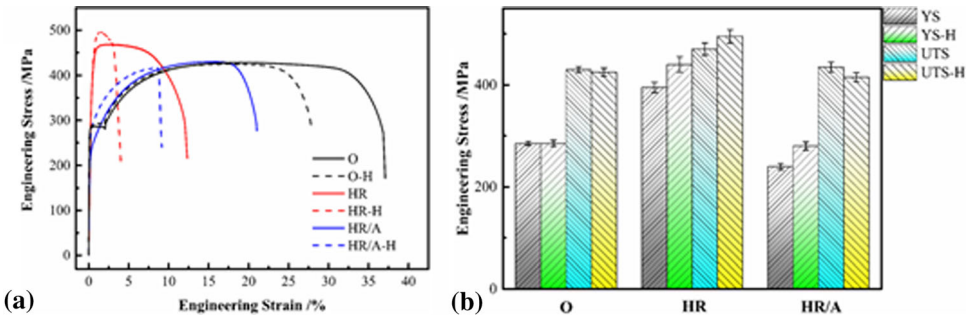

Fig. 5 (a) Stress–strain curves and (b) standard deviation of mechanical properties of specimens before and after hydrogen charging in different states

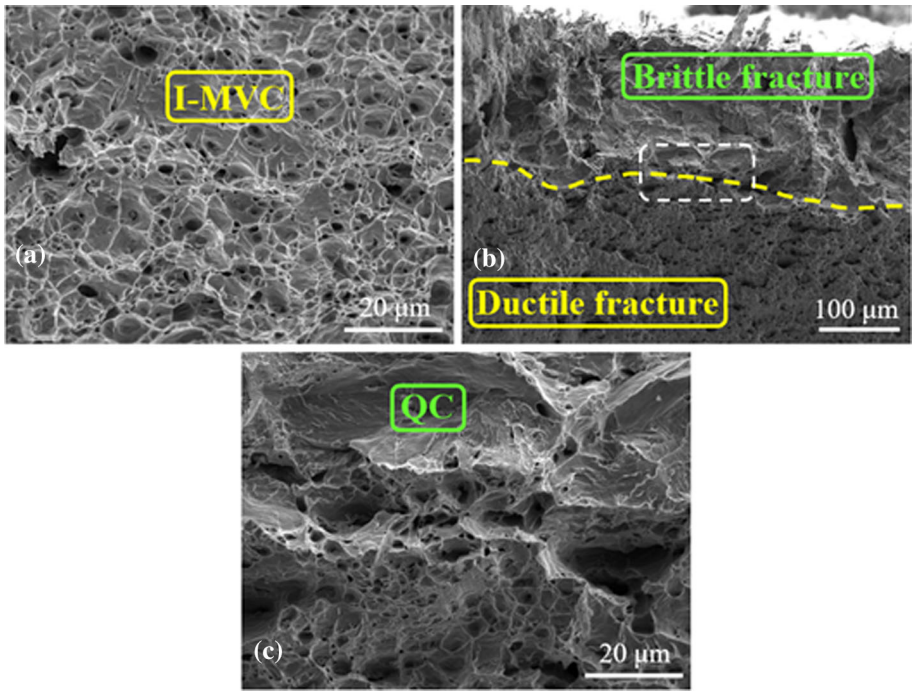

Fig. 6 Fracture morphology of original specimen. (a) Uncharged, (b) Hydrogen charging and (c) high-magnification image of the white wire frame in (b)

dislocations pinning (Ref 26-28). The influence of hydrogen on strength is more complicated and controversial (Ref 29-33). Hydrogen influence mechanism on the mechanical properties of the material has not been uniform; however, a large amount of literature has focused on the interaction between hydrogen and dislocations (Ref 34-37). Hydrogen trapped at a dislocation core, in a dilatational stress field, pins an edge dislocation (Ref 38). The hydrogen trapped by a dislocation increases the critical shear stress for dislocation glide, which is the main aspect that explains the increase in strength of the material after hydrogen charging (Ref 26). The plastic deformation of ferritic stainless steel is affected by many aspects (Ref 39). However, the stress–strain curve of the sample after hydrogen charging does not have the characteristic of the yield point, which is attributed to the complex relationship between hydrogen and dislocations. The accumulation of hydrogen atoms at the dislocations increases the yield strength of the material to a certain extent, while hydrogen atoms can also promote the movement of dislocations. Katzarov et al. (Ref 27) proved the interaction of hydrogen and dislocations under different conditions through modeling-hydrogen enhanced the dislocation mobility and hydrogen pinning effect. Hydrogen plays a vital role in increasing dislocation mobility. When the dislocation gets rid of the pinning effect of hydrogen atoms, the dislocation acts as an effective hydrogen trap, and the movement of the dislocation will be accompanied by the diffusion of hydrogen atoms. However, the exact mechanism by which hydrogen affects dislocation activity will still be an active part of the scientific debate (Ref 40).

3.3 Fractography

Fracture morphology and corresponding characteristic areas of the original specimen before and after hydrogen charging are displayed in Fig. 6. Many fine isometric dimples were observed at the fracture of the uncharged sample, as illustrated in Fig. 6a. After the introduction of hydrogen, the edge of the fracture surface of the original specimen exhibited brittle fracture features with an even and flat fracture surface in Fig. 6b. Moreover, in high-magnification image of the white wire frame in (b), it can be seen that the fracture mode of the original specimen changed from isometric-ductile micro-void coalescence (I-MVC) mode to Quasi-cleavage fracture (QC) mode after hydrogen charging. This is consistent with the observation of the fracture morphology of 17%Cr stainless steel by Tavares et al. (Ref 41). The center of the fracture remains ductility, which was characterized by coalesced micro-voids.

As demonstrated in Fig. 7, fracture morphology and corresponding characteristic areas of the hot-rolled specimen before and after hydrogen charging are displayed. Compared with the I-MVC fracture mode of the original specimen, the difference is that the fracture mode of the hot-rolled specimen is mainly tear-ductile micro-void coalescence (T-MVC) fracture, as illustrated in Fig. 7a. The dimensions and depth of dimples are different from the original specimen, which is attributed to the original sheet that is processed by the rolling process, and a large amount of stress is retained in the specimen, when the hot-rolled specimen is subjected to external force, the strain state of the crack tip in all directions during the crack propagation process is different. Figure 7b shows the typical fracture modes and region interfaces in ruptured hot-rolled specimen in the presence of hydrogen. Large and deep cracks primarily appeared in the grain boundaries, indicating that the fracture mode is mainly intergranular fracture (IG) in the presence of hydrogen. Figure 7c provides the corresponding high-magnification micrographs of the white wire frame in Fig. 7b. The fracture surface extends along the triple junction grain bound-

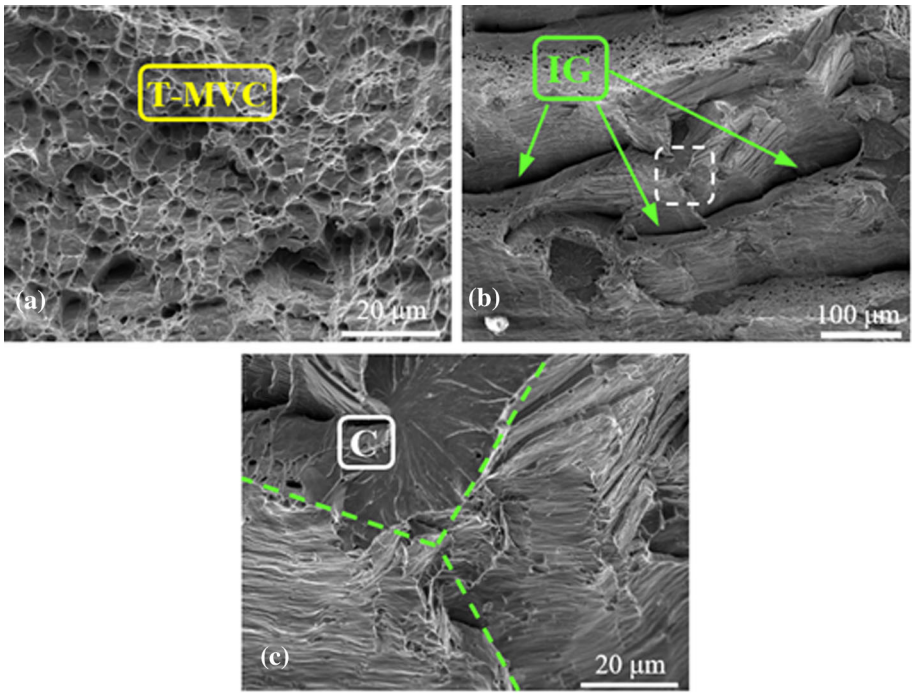

Fig. 7 Fracture morphology of hot-rolled specimen. (a) Uncharged, (b) Hydrogen charging and (c) high-magnification image of the white wire frame in (b)

aries, and the initial cracks in the cleavage zone nucleate at the grain boundaries and expand into the grains, indicating that cleavage fracture (C) exists simultaneously.

The macroscopic fractographies and corresponding characteristic areas of annealed specimens before and after hydrogen charging are displayed in Fig. 8. Comparing with the fracture surface of the uncharged specimen showing a representative necking phenomenon (Fig. 8a), the hydrogen-charged specimen exhibited brittle fracture features with an even and flat fracture surface without remarkable necking (Fig. 8b). In the high-magnification images of the microscopic fracture morphology in the white wire frame of Fig. 8a and b, respectively, it can be seen that uncharged specimen was dominated by I-MVC fractures, accompanied by T-MVC mode, the sample after hydrogen charging was dominated by C fracture, accompanied by QC mode at the cleavage torn edge (Fig. 8c), indicating that the annealing process effectively improved the internal stress state of the hot-rolled specimen. Due to the high strength of martensite and high sensitivity to hydrogen embrittlement, the initial cracks in the C zone originated from the grain boundaries.

4. Discussion

Typical brittle fracture characteristics are the main manifestations of HEDE mechanism-induced fracture, such as cleavage (C) fracture and intergranular (IG) fracture (Figs. 7b and 8d) (Ref 42). However, quasi-cleavage fracture (Fig. 8e), as a transition between ductile fracture and brittle fracture, is also a common feature of hydrogen-induced fracture and its fracture mode is not along a certain fracture surface. The propagation mechanism of hydrogen-induced cracks of specimens under different heat treatment states is summarized in Fig. 9. In electrochemical hydrogen charging process, due to the large deformation storage energy of the hot-rolled specimen (especially at the grain boundaries), hydrogen atoms were more easily stored, when the accumulation of hydrogen at a local location reaches the critical hydrogen concentration, the weakening between the grain boundaries and crystallographic planes leads to the formation of cracks and unstable growth. In addition, the nucleation of internal cracks in the material may also be attributed to the influence of hydrogen atom recombination. Hydrogen atoms induce superabundant vacancies, and the vacancies aggregate into hydrogen vacancy clusters (microcavities) (Ref 43). The recombination of hydrogen atoms in the microcavities leads to an increase in internal pressure. When the stress reaches cohesive strength, the crack nucleates and expands, which is all dominated by the HEDE mechanism. Turk et al. (Ref 10) revealed in the quantitative analysis of the hydrogen capture ability of the microstructure of multiphase steel that grain boundaries of the heavily deformed ferrite are more effective trapping sites than dislocations. This is consistent with the IG fracture observed in the hot-rolled specimen in Fig. 7b. The massive accumulation of hydrogen atoms at the grain boundaries of deformed ferrite leads to the formation of cracks, and the cracks extend along the grain boundaries (Ref 44) (Fig. 9c). After the hot-rolled specimen was processed by the annealing process, due to the release of the deformation and stored energy, the grain morphology changed to an equiaxed state. After hydrogen charging, the obvious change in the fracture morphology of the annealed specimen was attributed to the interaction of hydrogen and microstructure, including grain morphology, grain size and the formation of trace martensite phase at ferrite grain boundaries. Malitckii et al. (Ref 33)

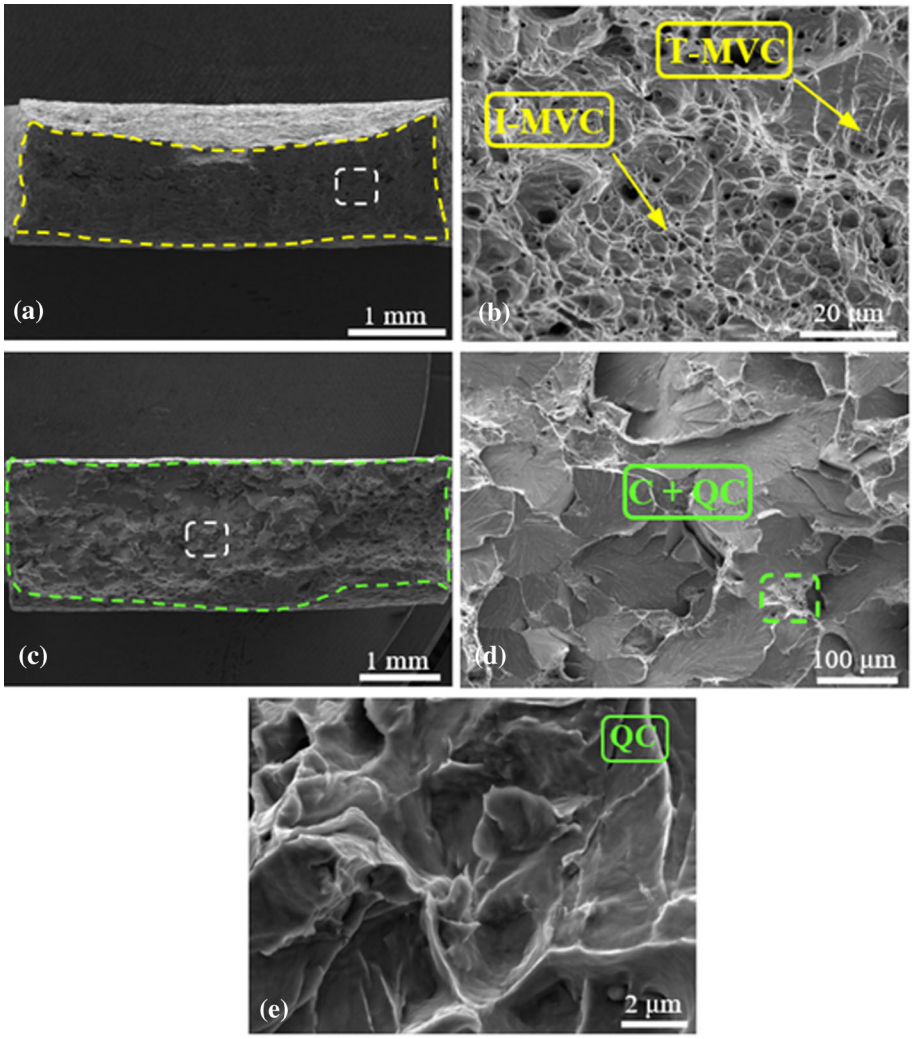

Fig. 8 Macroscopic fracture morphology of samples processed by hot rolling + annealing followed by (a) uncharged specimen and (b) Hydrogen charging specimen; (c) and (d) are high-magnification images of the microscopic fracture morphology in the white wire frame in (a) and (b), respectively; (e) is high-magnification image of the green wire frame in (d)

through researched hydrogen effects on mechanical properties of 18%Cr ferritic stainless steel and confirmed that the sensitivity to hydrogen embrittlement increases with the increase in the mean grain size. As a high-strength phase, martensite has a high dislocation density and a strong sensitivity to hydrogen embrittlement. Hydrogen promotes the movement of dislocations in the martensite phase leading to the formation of quasi-cleavage zones (Fig. 9d). The formation of cracks in the martensite phase is mainly due to the local excessively high hydrogen content leading to the weakening of the atomic binding energy between the lath martensite lamellae. The hydrogen-induced quasi-cleavage zone is located between brittle fracture and ductile fracture, which is the result of hydrogen effectively promoting local dislocation migration. In addition, the initial cracks in the cleavage zone were generated at the grain boundary, as the crack propagated the "river pattern" is formed. The internal cracks of the ferrite grains propagate along the specific interface ({001} crystal plane), which is attributed to the higher diffusible hydrogen content inside the ferrite. The tear ridges observed in the quasi-cleavage zone are the same as those reported by Martin et al. (Ref 45) and Nagao et al. (Ref 46). Fracture surfaces exhibit evidence for some small-scale ductile processes, which may be the result of hydrogen promoted dislocation movement, due to the HELP mechanism.

5. Conclusion

In this paper, the microstructure and fracture morphology of AISI 430 FSS subjected to various thermal conditions and corresponding the changes of fracture modes after hydrogen charging were investigated. The main conclusions obtained are as follows:

(1) The tensile test results show that in the presence of hydrogen, the specimens under different heat treatment conditions show obvious plastic loss. The HES_H of the HR specimen was the highest, and the HES_H of the HR

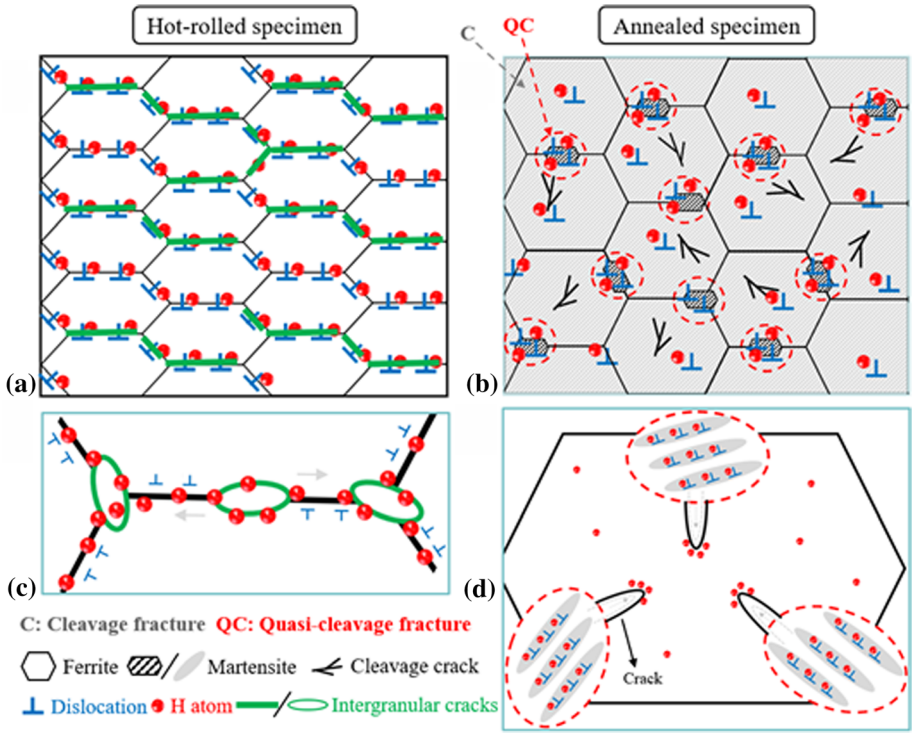

Fig. 9 Schematic diagram of propagation mechanisms of hydrogen-induced cracks under different heat treatment states. (c) and (d) correspond to the microscopic cracks of (a) and (b), respectively

specimen was reduced after the annealing process, which attributed to annealing improved the microstructure stress of the HR specimen and the local hydrogen pressure in the material was reduced.

(2) Hydrogen is sensitive to the microstructure characteristics of AISI 430 ferritic stainless steel, and the change of hydrogen on mechanical properties is attributed to the pinning effect of hydrogen on dislocations.

(3) In the study of hydrogen changing the fracture morphology, it was found that: the change of hydrogen embrittlement fracture mode of HR specimen is dominated by the HEDE mechanism, while the hydrogen embrittlement fracture of HR/A specimen is caused by the synergistic effect of HEDE and HELP mechanisms.

Acknowledgments

The authors wish to acknowledge the financial support of the Shanxi International Cooperation Project (Approval Number: 201603D421026).

References

1. S. Dutta, A Review on Production, Storage of Hydrogen and Its Utilization as an Energy Resource, *J. Ind. Eng. Chem.*, 2014, **20**(4), p 1148–1156.
2. X. Xing, R. Cheng, G. Cui, J. Liu, J. Gou, C. Yang, Z. Li and F. Yang, Quantification of the Temperature Threshold of Hydrogen Embrittlement in X90 Pipeline Steel, *Mater. Sci. Eng. A*, 2021, **800**, p 140118.
3. C. Zhou, B. Ye, Y. Song, T. Cui, P. Xu and L. Zhang, Effects of Internal Hydrogen and Surface-Absorbed Hydrogen on the Hydrogen Embrittlement of X80 Pipeline Steel, *Int. J. Hydrog. Energy*, 2019, **44**(40), p 22547–22558.
4. E. Ohaeri, J. Omale, K.M.M. Rahman and J. Szpunar, Effect of Post-processing Annealing Treatments on Microstructure Development and Hydrogen Embrittlement in API 5L X70 Pipeline Steel, *Mater. Charact.*, 2020, **161**, p 110124.
5. Q. Deng, W. Zhao, W. Jiang, T. Zhang, T. Li and Y. Zhao, Hydrogen Embrittlement Susceptibility and Safety Control of Reheated CGHAZ in X80 Welded Pipeline, *J. Mater. Eng. Perform.*, 2018, **27**(4), p 1654–1663.
6. X. Chen, L. Ma, C. Zhou, Y. Hong, H. Tao, J. Zheng and L. Zhang, Improved Resistance to Hydrogen Environment Embrittlement of Warm-Deformed 304 Austenitic Stainless Steel in High-pressure Hydrogen Atmosphere, *Corros. Sci.*, 2019, **148**, p 159–170.
7. I.M. Robertson, P. Sofronis, A. Nagao, M.L. Martin, S. Wang, D.W. Gross and K.E. Nygren, Hydrogen Embrittlement Understood, *Metall. Mater. Trans. B*, 2015, **46**(3), p 1085–1103.
8. S. Wang, A. Nagao, P. Sofronis and I.M. Robertson, Assessment of the Impact of Hydrogen on the Stress Developed Ahead of a Fatigue Crack, *Acta Mater.*, 2019, **174**, p 181–188.
9. C. Zhou, Q. Huang, Q. Guo, J. Zheng, X. Chen, J. Zhu and L. Zhang, Sulphide Stress Cracking Behaviour of the Dissimilar Metal Welded Joint of X60 Pipeline Steel and Inconel 625 Alloy, *Corros. Sci.*, 2016, **110**, p 242–252.
10. A. Turk, G.R. Joshi, M. Gintalas, M. Callisti, P.E.J. Rivera-Díaz-del-Castillo and E.I. Galindo-Nava, Quantification of Hydrogen Trapping in Multiphase Steels: Part I-Point Traps in Martensite, *Acta Mater.*, 2020, **194**, p 118–133.
11. A. Turk, S.D. Pu, D. Bombač, P.E.J. Rivera-Díaz-del-Castillo and E.I. Galindo-Nava, Quantification of Hydrogen Trapping in Multiphase Steels: Part II–Effect of Austenite Morphology, *Acta Mater.*, 2020, **197**, p 253–268.
12. C.D. Beachem, A New Model for Hydrogen-Assisted Cracking (hydrogen "embrittlement"), *Metall. Mater. Trans. B*, 1972, **3**(2), p 441–455.

13. A.R. Troiano, The Role of Hydrogen and Other Interstitials in the Mechanical Behavior of Metals, *Trans. Am. Soc. Met.*, 1960, **52**, p 54–80.
14. R.A. Oriani, Whitney Award Lecture-1987: Hydrogen-The Versatile Embrittler, *Corrosion*, 1987, **43**(7), p 390–397.
15. I.M. Robertson, The Effect of Hydrogen on Dislocation Dynamics, *Eng. Fract. Mech.*, 2001, **68**(6), p 671–692.
16. M. Wasim, M.B. Djukic and T.D. Ngo, Influence of Hydrogen-Enhanced Plasticity and Decohesion Mechanisms of Hydrogen Embrittlement on the Fracture Resistance of Steel, *Eng. Fail. Anal.*, 2021, **123**, p 105312.
17. M.B. Djukic, G.M. Bakic, V.S. Zeravcic, A. Sedmak and B. Rajicic, The Synergistic Action and Interplay of Hydrogen Embrittlement Mechanisms in Steels and Iron: Localized Plasticity and Decohesion, *Eng. Fract. Mech.*, 2019, **216**, p 106528.
18. Y. Ogawa, D. Birenis, H. Matsunaga, O. Takakuwa, J. Yamabe, Ø. Prytz and A. Thøgersen, The Role of Intergranular Fracture on Hydrogen-Assisted Fatigue Crack Propagation in Pure Iron at a Low Stress Intensity Range, *Mater. Sci. Eng. A*, 2018, **733**, p 316–328.
19. P. Novak, R. Yuan, B.P. Somerday, P. Sofronis and R.O. Ritchie, A Statistical, Physical-Based, Micro-mechanical Model of Hydrogen-Induced Intergranular Fracture in Steel, *J. Mech. Phys. Solids*, 2010, **58**(2), p 206–226.
20. M. Koyama, C.C. Tasan, E. Akiyama, K. Tsuzaki and D. Raabe, Hydrogen-Assisted Decohesion and Localized Plasticity in Dual-phase Steel, *Acta Mater.*, 2014, **70**, p 174–187.
21. M. Jedrychowski, J. Tarasiuk, B. Bacroix and S. Wronski, Electron Backscatter Diffraction Investigation of Local Misorientations and Orientation Gradients in Connection with Evolution of Grain Boundary Structures in Deformed and Annealed Zirconium. A New Approach in Grain Boundary Analysis, *J. Appl. Crystallogr.*, 2013, **753**, p 93–96.
22. M. Calcagnotto, D. Ponge, E. Demir and D. Raabe, Orientation Gradients and Geometrically Necessary Dislocations in Ultrafine Grained Dual-phase Steels Studied by 2D and 3D EBSD, *Mater. Sci. Eng. A*, 2010, **527**(10), p 2738–2746.
23. Q. Liu and N. Hansen, Geometrically Necessary Boundaries and Incidental Dislocation Boundaries Formed During Cold Deformation, *Scr. Metall. Mater.*, 1995, **32**(8), p 1289–1295.
24. J. Lufrano and P. Sofronis, Enhanced Hydrogen Concentrations Ahead of Rounded Notches and Cracks-Competition Between Plastic Strain and Hydrostatic Stress, *Acta Mater.*, 1998, **46**(5), p 1519–1526.
25. N. Bandyopadhyay, J. Kameda and C.J. McMahon, Hydrogen-Induced Cracking in 4340-type Steel: Effects of Composition, Yield Strength, and H2 Pressure, *Metall. Trans. A*, 1983, **14**(4), p 881–888.
26. Y. Murakami, T. Kanezaki and Y. Mine, Hydrogen Effect against Hydrogen Embrittlement, *Metall. Mater. Trans. A*, 2010, **41**(10), p 2548–2562.
27. I.H. Katzarov, D.L. Pashov and A.T. Paxton, Hydrogen Embrittlement I. Analysis of Hydrogen-Enhanced Localized Plasticity: Effect of Hydrogen on the Velocity of Screw Dislocations in α-Fe, *Phys. Rev. Mater.*, 2017, **1**(3), p 033602.
28. S. Taketomi, R. Matsumoto and S. Hagihara, Molecular Statics Simulation of the Effect of Hydrogen Concentration on 112 < 111 > Edge Dislocation Mobility in Alpha Iron, *ISIJ Int.*, 2017, **57**(11), p 2058–2064.
29. W.J. Qi, R.G. Song, X. Qi, H. Li, Z.X. Wang, C. Wang and J.R. Jin, Hydrogen Embrittlement Susceptibility and Hydrogen-Induced Additive Stress of 7050 Aluminum Alloy Under Various Aging States, *J. Mater. Eng. Perform.*, 2015, **24**(9), p 3343–3355.
30. M. Okayasu and T. Fujiwara, Effects of Microstructural Characteristics on the Hydrogen Embrittlement Characteristics of Austenitic, Ferritic, and γ–α Duplex Stainless Steels, *Mater. Sci. Eng. A*, 2021, **807**, p 140851.
31. C.L. Lai, L.W. Tsay and C. Chen, Effect of Microstructure on Hydrogen Embrittlement of Various Stainless Steels, *Mater. Sci. Eng. A*, 2013, **584**, p 14–20.
32. D. Zhou, T. Li, D. Huang, Y. Wu, Z. Huang, W. Xiao, Q. Wang and X. Wang, The Experiment Study to Assess the Impact of Hydrogen Blended Natural Gas on the Tensile Properties and Damage Mechanism of X80 Pipeline Steel, *Int. J. Hydrog. Energy*, 2021, **46**(10), p 7402–7414.
33. E. Malitckii, Y. Yagodzinskyy, P. Lehto, H. Remes, J. Romu and H. Hänninen, Hydrogen Effects on Mechanical Properties of 18%Cr Ferritic Stainless Steel, *Mater. Sci. Eng. A*, 2017, **700**, p 331–337
34. M. Maxelon, A. Pundt, W. Pyckhout-Hintzen and R. Kirchheim, Small Angle Neutron Scattering of Hydrogen Segregation at Dislocations in Palladium, *Scr. Mater.*, 2001, **44**(5), p 817–822
35. R. Kirchheim, Reducing Grain Boundary, Dislocation Line and Vacancy Formation Energies by Solute Segregation: II. Experimental Evidence and Consequences, *Acta Mater.*, 2007, **55**(15), p 5139–5148
36. V.G. Gavriljuk, V.N. Shivanyuk and J. Foct, Diagnostic Experimental Results on the Hydrogen Embrittlement of Austenitic Steels, *Acta Mater.*, 2003, **51**(5), p 1293–1305.
37. V.G. Gavriljuk, V.N. Shivanyuk and B.D. Shanina, Change in the Electron Structure Caused by C, N and H Atoms in Iron and Its Effect on their Interaction with Dislocations, *Acta Mater.*, 2005, **53**(19), p 5017–5024.
38. S. Moriya, H. Matsui and H. Kimura, The Effect of Hydrogen on the Mechanical Properties of High Purity Iron II. Effect of Quenched-in Hydrogen Below Room Temperature, *Mater. Sci. Eng.*, 1979, **40**(2), p 217–225.
39. O. Di Pietro, G. Napoli, M. Gaggiotti, R. Marini, G. Stornelli and A. Schino, Analysis of Plastic Forming Parameters In Aisi 441 Stainless Steel, *Acta Metall. Slovaca*, 2020, **26**, p 178–183.
40. M.L. Martin, M.J. Connolly, F.W. DelRio and A.J. Slifka, Hydrogen Embrittlement in Ferritic Steels, *Appl. Phys. Rev.*, 2020, **7**(4), p 041301.
41. S.S.M. Tavares, I.N. Bastos, J.M. Pardal, T.R. Montenegro and M.R. da Silva, Slow Strain Rate Tensile Test Results of New Multiphase 17%Cr Stainless Steel Under Hydrogen Cathodic Charging, *Int. J. Hydrog. Energy*, 2015, **40**(47), p 16992–16999.
42. R. Kirchheim, Revisiting Hydrogen Embrittlement Models and Hydrogen-Induced Homogeneous Nucleation of Dislocations, *Scr. Mater.*, 2010, **62**(2), p 67–70.
43. X. Ren, Q. Zhou, W. Chu, J. Li, Y. Su and L. Qiao, The Mechanism of Nucleation of Hydrogen Blister in Metals, *Chinese Sci. Bull.*, 2007, **52**(14), p 2000–2005.
44. S. Wang, M.L. Martin, P. Sofronis, S. Ohnuki, N. Hashimoto and I.M. Robertson, Hydrogen-Induced Intergranular Failure of Iron, *Acta Mater.*, 2014, **69**, p 275–282.
45. M.L. Martin, J.A. Fenske, G.S. Liu, P. Sofronis and I.M. Robertson, On the Formation and Nature of Quasi-Cleavage Fracture Surfaces in Hydrogen Embrittled Steels, *Acta Mater.*, 2011, **59**(4), p 1601–1606.
46. A. Nagao, C.D. Smith, M. Dadfarnia, P. Sofronis and I.M. Robertson, The Role of Hydrogen in Hydrogen Embrittlement Fracture of Lath Martensitic Steel, *Acta Mater.*, 2012, **60**(13), p 5182–5189.